Journal of
Materials Chemistry A

ROYAL SOCIETY
OF CHEMISTRY

PAPER

View Article Online
View Journal | View Issue

Check for updates

Cite this: J. Mater. Chem. A, 2022, 10, 19839

# $MgH_2$/single-atom heterojunctions: effective hydrogen storage materials with facile dehydrogenation†

Shuai Dong,[a] Chaoqun Li,[a] Erfei Lv,[a] Jinhui Wang,[a] Hao Liu,[a] Zhengyang Gao,[a] Wei Xiong, *[b] Zhao Ding,[c] Weijie Yang *[a] and Hao Li *[d]

Received 17th March 2022
Accepted 9th May 2022

DOI: 10.1039/d2ta02111k

rsc.li/materials-a

Magnesium hydride ($MgH_2$) is considered as a promising solid-state hydrogen storage material due to its high hydrogen storage mass density and environmental friendliness. However, its sluggish dehydrogenation kinetics are still the bottleneck that restricts practical applications. To address this challenge, very recent pioneering experiments found that $MgH_2$/single-atom catalyst ($MgH_2$/SAC) heterojunctions can be promising candidates for hydrogen storage. However, the reaction mechanism and design guideline were still not well understood. Herein, we design and analyze $MgH_2$/SAC heterojunction systems including nine 3d transition metals, using spin-polarized density functional theory calculations with van der Waals corrections. We found that the energy barriers of $MgH_2$ dehydrogenation are significantly reduced by 0.51–2.22 eV through the promotion effects of a heterojunction. Using *ab initio* molecular dynamics simulations, these promotion effects were analyzed in depth based on the observation of hydrogen diffusion behaviors. To provide further insights, the electron localization function, charge density difference, hydrogen adsorption energy, system electronegativity, d-band center, and crystal orbital Hamilton population were comprehensively analyzed to understand the origin of the high performance of $MgH_2$/SACs. In particular, we found that the system electronegativity of SACs can act as an effective descriptor that predicts the dehydrogenation energy barriers. Most importantly, this study provides important design guidelines of a brand-new type of $MgH_2$/SAC material and a promising solution to the sluggish kinetics of $MgH_2$ dehydrogenation in hydrogen storage.

---

[a] *School of Energy and Power Engineering, North China Electric Power University, Baoding, 071003, China. E-mail: yangwj@ncepu.edu.cn*

[b] *Key Laboratory for Green Chemical Process (Ministry of Education), Engineering Research Center of Phosphorus Resources Development and Utilization of Ministry of Education, Hubei Key Laboratory of Novel Reactor & Green Chemical Technology, School of Chemistry and Environmental Engineering, Wuhan Institute of Technology, Wuhan 430205, China. E-mail: xiongwei@wit.edu.cn*

[c] *College of Materials Science and Engineering, Chongqing University, Chongqing, 400044, China*

[d] *Advanced Institute for Materials Research (WPI-AIMR), Tohoku University, Sendai 980-8577, Japan. E-mail: li.hao.b8@tohoku.ac.jp*

† Electronic supplementary information (ESI) available. See https://doi.org/10.1039/d2ta02111k

---

*Prof. Wei Xiong received his PhD degree in Physical Chemistry from Tongji University, China, in 2012. At present, he works as an Associate Professor in the School of Chemistry and Environmental Engineering at Wuhan Institute of Technology. His main research interests include nanomaterials for energy and environmental applications, such as hydrogen storage, supercapacitors, electrocatalytic nitrogen reduction, electrochemical sensors, theoretical calculation, etc. He has published over 20 original research papers in materials, chemistry, and energy related journals.*

## Introduction

Hydrogen is a green energy source in industry.[1–3] However, how to safely and effectively use hydrogen are the main challenges that hinder its broad utilization.[4–6] Among the gas–liquid–solid three-phase materials, solid hydrogen storage materials not only have the advantages of high safety but also high volumetric energy density.[7–9] Among solid hydrogen storage materials, light metal hydrides are ideal candidates as hydrogen storage materials due to their high storage capacity.[10–12] Magnesium hydride ($MgH_2$) (7.6 wt%) has good reversibility and low cost, which make it a potential hydrogen storage material.[13,14] However, the experimental dehydrogenation enthalpy of magnesium is high.[15] Due to the key challenge in the dehydrogenation process, its working temperature is 450–550 °C in practical applications, making it difficult to apply it in the energy industry.[16]

Common strategies to address these challenges include alloying,[17–22] nanostructuring,[23–27] and doping.[28–39] Among these strategies, doping can significantly improve the dehydrogenation performance because it may accelerate hydrogen transfer.[4] At present, transition metal based materials with high activity are considered as ideal dopants, most of which are metals and metal compounds.[4,14,28–38] Because the weight of metals is larger than that of non-metals, the material weight is greatly increased, and therefore the hydrogen storage capacity is limited. Even if the material has a good hydrogen storage performance, it is difficult to use it in industry due to the relatively high weight. Moreover, the coordination saturation of those catalysts is insufficient to activate $MgH_2$, leading to a high dehydrogenation temperature which cannot meet the urgent needs in engineering. Therefore, it is particularly important to search for a hydrogen storage material with both light weight and high performance.

The emergence of metal–carbon composites[36,39–41] is one of the promising solutions to this challenge. Carbon-based single-atom catalysts (SACs) can further reduce the relative mass, which endows them with unique advantages as dehydrogenation catalysts. SACs have a maximum atom utilization[42–48] and excellent performance in many catalytic processes, including oxygen reduction,[49,50] oxygen evolution,[51] nitrogen reduction,[52–57] $CO_2$ reduction,[58–60] and hydrogen-involving reactions such as organic dehydrogenation/hydrogenation[61–66] and the hydrogen evolution reaction.[67–72] Since hydrogen storage has a similar hydrogen transfer process, it can be reasonably expected that the introduction of SACs onto $MgH_2$ may improve its dehydrogenation/hydrogenation performance. Transition metal and nitrogen-doped carbon composites (TM–N–C, where TM = Fe, Co, Ni, Cu, *etc.*) were first reported by the Zhang group and found to be promising candidates for many applications.[42] Very recently, Huang *et al.*[73] analyzed the SACs with a TM–N–C structure and found that these materials could significantly promote the dehydrogenation performance of $MgH_2$ for hydrogen storage. They showed that the hydrogen storage capacity of the material was about 5.4 wt%. Given that the hydrogen storage capacity between 5 wt% and 15 wt% can be considered as a high hydrogen storage performance, the study of this type of material is of great significance. They used a quasi-solid-state template method involving ball-milling, calcination, and washing to synthesize highly disperse SACs. The composite materials formed by adding these SACs onto $MgH_2$ showed excellent hydrogen storage and dehydrogenation performance. This pioneering study published in the year 2021 provides a brand-new avenue to address the challenges of $MgH_2$ dehydrogenation. However, related mechanistic understanding and design guidelines are still not clear.

Motivated by the very recent success from experiments and the remaining challenges, herein, first-principles calculations were employed to analyze the reaction pathways and related kinetics and thermodynamics of $MgH_2$ and nine $MgH_2$/SAC heterojunction systems. The materials with promising dehydrogenation performances were then selected for electronic structure analysis and *ab initio* molecular dynamics (AIMD) simulations. Subsequently, we comprehensively analyzed the structure–property relationships of $MgH_2$/SAC heterojunction systems and generalized the trends in their dehydrogenation performance. Finally, we provided a design guideline for $MgH_2$/SAC heterojunctions as high-performance hydrogen storage materials and screened other SAC candidates among 3d, 4d, and 5d transition metals in the periodic table.

## Computational and modeling methods

### Computational methods

Density functional theory (DFT) calculations were performed using the Vienna *Ab initio* Simulation Package (VASP) with the projector augmented wave (PAW) method. The Perdew–Burke–Ernzerhof (PBE) functional within the generalized gradient approximation (GGA) was employed to describe the exchange–correlation energy.[74–76] Previous benchmarking studies and related discussions showed that PBE is relatively precise for describing hydrogen adsorption and desorption,[77,78] in good agreement with ultrahigh vacuum experimental results. Meanwhile, we also considered both spin-polarization[79] and van der Waals corrections using the DFT-D3 scheme.[80] Dipole moments were corrected along the *z*-direction for all the calculations. A plane-wave basis set with an energy cutoff of 450 eV was used to describe valence electrons. The geometries were considered relaxed when all the forces of each atom decreased below 0.05 eV $\text{Å}^{-1}$. A $(4 \times 4 \times 1)$ $\Gamma$-centered *k*-point grid was employed for structural relaxations (Fig. S1†). All geometry optimizations were performed using the conjugate gradient method. The climbing-image nudged elastic band (CI-NEB) method developed by Henkelman *et al.*[81,82] was employed to locate the transition states (TS) of dehydrogenation reactions. The image number of the CI-NEB calculations was obtained based on a calculated reference value: the VASP-VTST[83] script calculated the atomic distance between the initial and final states (IS and FS, respectively), after which we specified that the distance between two adjacent images was less than 0.8 Å, thus obtaining a reference value for the number of our CI-NEB images. As a result, at least four images were inserted between the IS and FS in our study to locate the TS using CI-NEB calculations. AIMD simulations embedded in the VASP code were performed with a time step of 1 fs with a simulation duration of 10 000 steps, *i.e.*, 10 ps, in the NVT ensemble using the Nose–Hoover thermostat. According to previous studies, the dehydrogenation temperature of $MgH_2$ was around 663 K.[84] At this point, we chose 500 K for the AIMD simulation of $MgH_2$ and $MgH_2$/SAC. This allows a better comparison of the kinetic gap between pure $MgH_2$ and $MgH_2$/SAC. The visualization software VMD was used for the post-processing of AIMD.[85] To determine whether the single-atom site is stable at the heterojunction structure, the binding energies of the single-atom transition metals were calculated *via* the following equation:

$$E_{\mathrm{b}} = E_{\mathrm{SAC}} - E_{\mathrm{TM}} - E_{\mathrm{CN}} \tag{1}$$

where $E_{\mathrm{b}}$ is the binding energy, $E_{\mathrm{SAC}}$ is the total energy of the catalyst, $E_{\mathrm{TM}}$ is the total energy of the single-atom transition metals in a vacuum, and $E_{\mathrm{CN}}$ is the energy of N-doped graphene substrates without the single-atom.

In addition, to further estimate the dehydrogenation temperature from the resulting energy barriers, we invoked the Arrhenius equation:[86]

$$v = v^{*} \exp\left(-\frac{E_{\mathrm{ac}}}{k_{\mathrm{B}}T}\right) \tag{2}$$

where $v$ is the rate constant, $v^{*}$ is the prefactor, and $E_{\mathrm{ac}}$ is the activation energy.

To explore the magnitude of the hydrogen adsorption capacity of the catalyst, we introduced the H adsorption energies ($E_{\mathrm{H}}$), which were calculated as follows:

$$E_{\mathrm{H}} = E_{\mathrm{tot}} - E_{\mathrm{SAC}} - E_{\mathrm{hydrogen}} \tag{3}$$

where $E_{\mathrm{tot}}$ is the total energy of the hydrogen adsorption system, $E_{\mathrm{SAC}}$ is the energy of the catalyst, and $E_{\mathrm{hydrogen}}$ is the energy of hydrogen, which is half of the energy of one hydrogen molecule. To better describe the charge of metal atoms in SACs, system electronegativity ($X$)[87] was introduced as a charge descriptor based on the atomic electronegativity.[88] This helps analyze the contribution of adjacent atoms of metal atoms. In this study, $X$ was calculated using the following equation:

$$X = (xX_{\mathrm{C}} + yX_{\mathrm{N}} - X_{\mathrm{M}}) \times \frac{\theta_{\mathrm{d}}}{n_{\mathrm{d}}} \tag{4}$$

where $x$ is the number of carbon atoms adjacent to the embedded metal, $X_{\mathrm{C}}$ is the electronegativity of carbon, $y$ is the number of nitrogen atoms adjacent to the embedded metal, $X_{\mathrm{N}}$ is the electronegativity of nitrogen, $X_{\mathrm{M}}$ is the electronegativity of the embedded metal, $\theta_{\mathrm{d}}$ is the number of electrons occupied in the d-orbital, and $n_{\mathrm{d}}$ is the largest number of electrons in the d-orbital. We also introduced the d-band center[89] in the correlation and electronic structure analyses, which was calculated as follows:

$$\varepsilon_{\mathrm{d}} = \frac{\int_{-\infty}^{+\infty} ED(E)\mathrm{d}E}{\int_{-\infty}^{+\infty} D(E)\mathrm{d}E} \tag{5}$$

where $D(E)$ is the total d states of the metal atom in SACs.

To analyze the charge change upon the addition of SACs, we calculated the charge density difference ($\Delta\rho$). Charge density difference is one of the important ways to analyze electronic structures, which was calculated by the following equation:

$$\Delta\rho = \rho_{\mathrm{AB}} - \rho_{\mathrm{A}} - \rho_{\mathrm{B}} \tag{6}$$

where $\Delta\rho$ represents the change value in charge density, $\rho_{\mathrm{AB}}$ represents the charge density when two fragments of A and B are together, and $\rho_{\mathrm{A}}$ and $\rho_{\mathrm{B}}$ respectively represent the charge densities when A and B are individually present at the same position. To analyze the stability of chemical bonds in the system, the crystal orbital Hamiltonian population (COHP) method was employed,[90,91] which was calculated using the LOBSTER package.[92,93]

### Modeling methods

The initial configuration of the $MgH_2$ surface was cleaved from the rutile structure of bulk $MgH_2$. To analyze the effects of single-atom metals on the catalytic performance, nine 3d transition metals (Ti, V, Cr, Mn, Fe, Co, Ni, Cu, and Zn) were explicitly analyzed as the SACs in this study (Fig. 1a). All $MgH_2$ surfaces in this study were modeled as a stable (110) slab due its low surface energy,[94] with (4 × 4) unit cells (Fig. 1b). Only the dehydrogenation energy barrier on the $MgH_2$ surface was calculated, and there are only two types of H atoms at the surface: bridge and sub-bridge hydrogen. The studied dehydrogenation process is a reaction using two bridge hydrogens (BH) to generate a hydrogen molecule. Based on the most widely seen SAC structures from experiments,[73] the single-atoms were embedded at the $-N_4$ sites of a defected graphene surface. To build a heterojunction with the surface of $MgH_2$(110), the dimension size of single-atom doped graphene was adjusted to 12.62 × 12.68 Å to minimize lattice mismatch (Fig. 1c). A vacuum layer of 15 Å was set in the $z$-direction to separate images. After optimization, the gap between $MgH_2$ and SACs was found to be 3.00 Å (Table S1†). A side view of the $MgH_2$/SAC heterojunction considered for our calculations is shown in Fig. 1d.

## Results and discussion

### $MgH_2$ dehydrogenation at $MgH_2$ and $MgH_2$/SAC heterojunctions

To analyze the stability of the catalysts, we calculated the binding energy of the transition metal SAs at the $-N_4$–C site (Table 1); the results showed that the binding energies were all very negative, suggesting that these SACs are thermodynamically stable in the heterojunction system. Also, after structural optimization for all the heterojunction systems, we found that the metal atoms always face the side with H atoms after relaxation. Firstly, we analyzed the dehydrogenation kinetics of $MgH_2$ for comparison (Fig. 2a, red lines). The associative desorption of two bridging atomic H at the top layer has a reaction energy and activation energy barrier of 2.78 and 3.44 eV, respectively. Previous studies found that pure graphene

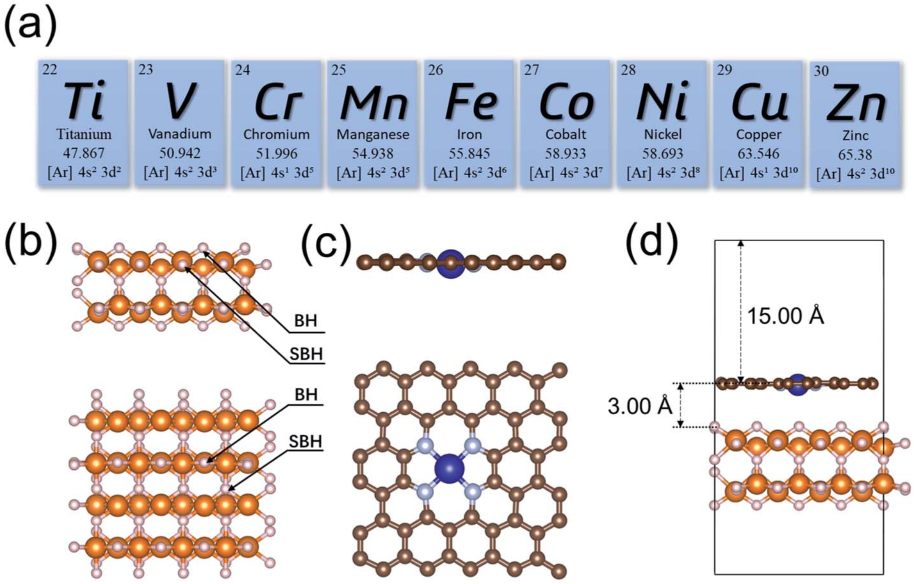

Fig. 1 (a) The 3d transition metal elements (Ti, V, Cr, Mn, Fe, Co, Ni, Cu, and Zn) considered as the single-atom dopant analyzed in our study. (b and c) Illustrations of the optimized structures considered for calculations. White and orange spheres represent H and Mg, respectively. Brown, gray, and blue spheres represent C, N, and Cr, respectively. (b) Side and top views of the $MgH_2(110)$ surface. BH and SBH represent bridge and sub-bridge hydrogen, respectively. (c) Side and top views of a structure of SAC, using Cr as an example. (d) Side view of an $MgH_2$/SAC heterojunction.

is incapable of affecting $MgH_2$ dehydrogenation.[95] Therefore, any performance variation of $MgH_2$/SACs is mainly contributed by the doping of single-atom metals. The free energy diagrams (where the zero-point energy corrections and entropic changes were included) and corresponding structures of $MgH_2$ and $MgH_2$/SAC heterojunctions are shown in Fig. 2, with the calculated data tabulated in Tables S2–S4.† The final and transition state structures of different systems are slightly different, mainly due to different positions of doped metal atoms in the catalysts and the dissociation order of H in the transition states. Interestingly, the results show that when SACs are added above $MgH_2$, both the energy barriers and reaction energies of $MgH_2$ dehydrogenation are reduced at all nine SACs. Moreover, the hydrogen evolution pathway of $MgH_2$ changes significantly after the addition of SACs (Fig. 2b). From the obtained energy barriers, we can estimate the relative decrease of reaction temperature. According to the Arrhenius equation, when the dehydrogenation temperature of $MgH_2$ is assumed to be 700 K, the dehydrogenation temperature for the same reaction rate constant of other systems can be estimated (Table S5†), and the lowest dehydrogenation temperature obtained is 247.65 K at $MgH_2$/SAC–Ti. Since the dehydrogenation energy barriers of pure magnesium hydride obtained from different articles[95–98] are different, we use the reduction percentage of dehydrogenation energy barriers for comparison (Table S6†). We found that $MgH_2$/SAC–Ti has a larger reduction percentage of dehydrogenation energy barrier than the previously analyzed materials. These results clearly indicate that SACs have a significant effect on the optimization of the hydrogen storage performance of $MgH_2$. Among them, the decrease in the energy barrier is most pronounced when Ti is the dopant, and it is lower than half of the dehydrogenation energy barrier of pure $MgH_2$. In addition, the order of thermodynamic energy changes is in good agreement with the magnitude of the energy barriers. Besides, it

Table 1 Calculated values of the binding energy of the single-atom transition metal ($E_b$), energy barriers ($E_a$), the height of metal after relaxation ($H_M$), the difference of metal charge ($\Delta Q_M$), the difference of N charge ($\Delta Q_N$), H adsorption energy ($E_H$), system electronegativity, and d-band center ($\varepsilon_d$) of SACs in the $MgH_2$/SAC heterojunctions

| Metal | $E_b$ (eV) | $E_a$ (eV) | $H_M$ (Å) | $\Delta Q_M$ (e) | $\Delta Q_N$ (e) | $E_H$ (eV) | Electronegativity | $\varepsilon_d$ (eV) |
|---|---|---|---|---|---|---|---|---|
| Ti | −7.732 | 1.217 | 0.924 | −1.383 | 0.892 | −0.116 | −0.116 | 0.308 |
| V | −8.296 | 1.706 | 0.812 | −1.310 | 1.008 | −0.050 | −0.050 | 0.220 |
| Cr | −4.639 | 1.656 | 0.520 | −1.243 | 0.986 | −0.308 | −0.308 | −0.191 |
| Mn | −6.041 | 1.756 | 0.173 | −1.292 | 1.049 | −0.280 | −0.280 | −0.963 |
| Fe | −7.426 | 1.563 | 0.254 | −1.088 | 0.911 | −0.675 | −0.675 | −0.898 |
| Co | −7.134 | 2.253 | 0.043 | −0.848 | 0.521 | −0.150 | −0.150 | −0.701 |
| Ni | −8.058 | 2.909 | 0.077 | −0.847 | 0.619 | −0.149 | −0.149 | −1.746 |
| Cu | −4.607 | 2.690 | 0.010 | −0.928 | 0.861 | −0.230 | −0.230 | −3.294 |
| Zn | −2.430 | 2.596 | 0.290 | −1.142 | 1.168 | −0.219 | −0.219 | −6.069 |

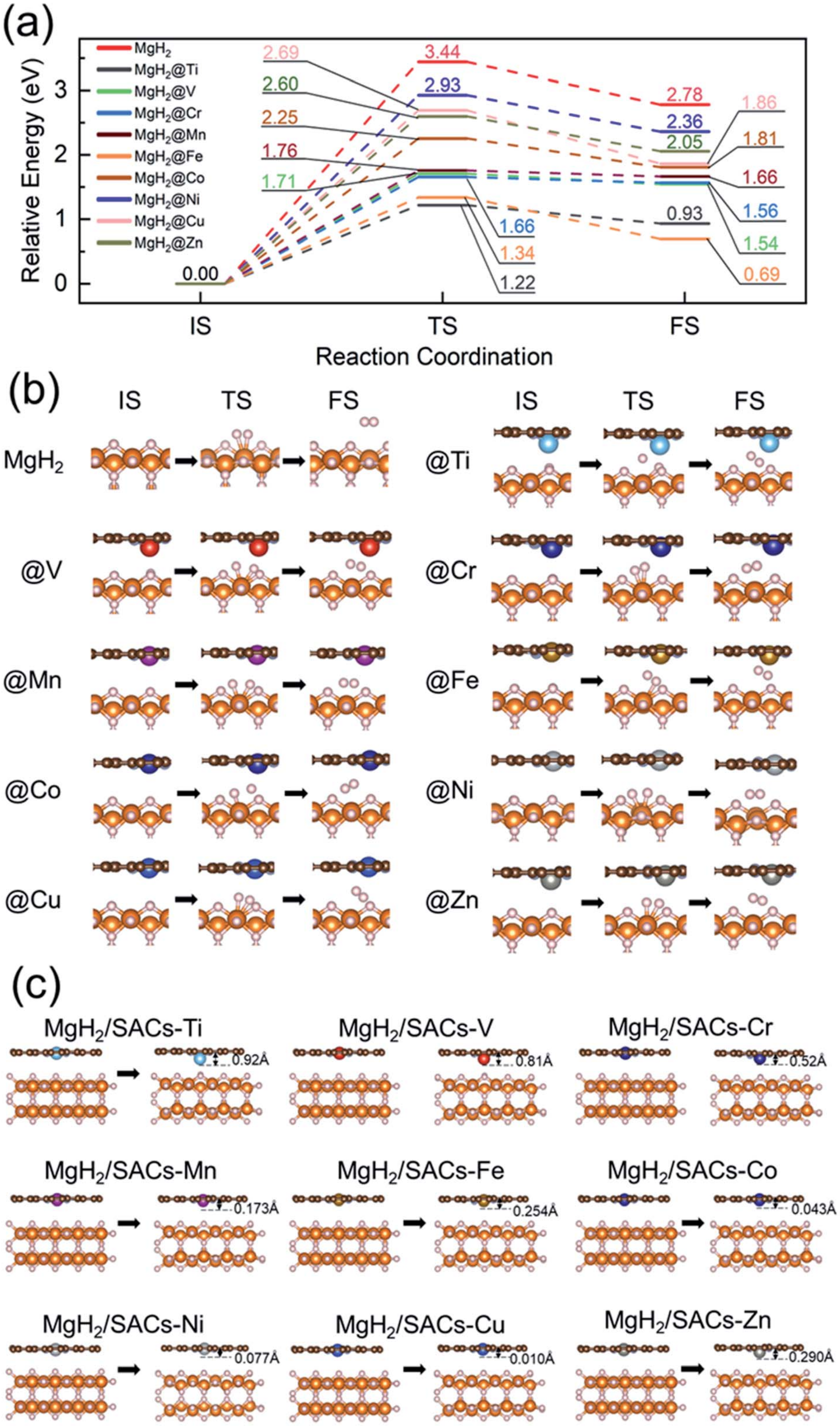

Fig. 2 (a) Free energy profiles of $MgH_2$ dehydrogenation at $MgH_2$ and nine $MgH_2$/SAC–TM (TM = Ti, V, Cr, Mn, Fe, Co, Ni, Cu, and Zn) heterojunction systems. (b) Initial, transition, and final states (IS, TS, and FS) of dehydrogenation at $MgH_2$ and $MgH_2$/SACs. White, orange, brown, and gray spheres represent H, Mg, C, and N, respectively. (c) Illustrations of the changes of metal atom height after structural relaxation of SACs in the heterojunctions. The distance marked at the top right of the model is the displacement distance of the transition metal atoms. For ease of understanding, in the free energy diagrams, we only show the IS, TS, and FS images of the whole process.

was found from the optimized structures that some of the SACs have significant displacements with their single-atom metals moving closer towards $MgH_2$ after structural relaxation (Fig. 2c).

## Analysis of structure–property relationships

To investigate the relevance between SACs and their reaction kinetics and thermodynamics, we analyzed the height change of metal atoms, metal charge difference, N charge difference, H adsorption energy, system electronegativity, and d-band center of these SACs in the heterojunctions (Table 1). Based on the information in Table 1, we carried out Pearson correlation coefficient (PCC) analysis to discuss their correlations with the dehydrogenation energy barriers of $MgH_2$ (Fig. 3a). Among the six properties, the system electronegativity correlates most significantly with dehydrogenation energy barriers, with a correlation coefficient of 0.88. Therefore, we plotted the linear correlation between energy barrier and electronegativity in Fig. 3b. According to statistical theory,[99] an $R^2$ of 0.83 (Fig. 3b) suggests a relatively high correlation between the two variables. Electronegativity is an important charge descriptor based on the atoms' atomic electronegativity (eqn (1)),[88] which has been used to understand the reactivity of the atom center of SACs.[87] As shown in Fig. 3b, the energy barrier increases with the increase of the electronegativity of SACs. This is because the two atomic H are negatively charged in $MgH_2$, making it difficult for them to form $H_2$. The charge distribution of H is affected by the charge properties of the single-atom metals, leading to a more facile bonding between two atomic H. These results are in good agreement with the previous experimental conclusion that metal electronegativity is highly correlated with the dehydrogenation kinetics.[73] However, in the previous study,[73] the order of electronegativity was not fully the same as the order of energy barriers, which is less precise than our analyses presented here. According to previous analyses,[100] the experimentally prepared metal-doped graphene has uncertainty and irregularity in structure, and the N-coordination numbers of each dopant atom were usually not identical in this type of material. Moreover, the N-coordination number directly affects the catalytic properties of the material,[50,101] which is one of the main reasons leading to the discrepancy of the data between this paper and the previous experimental material.[73] Therefore, previous

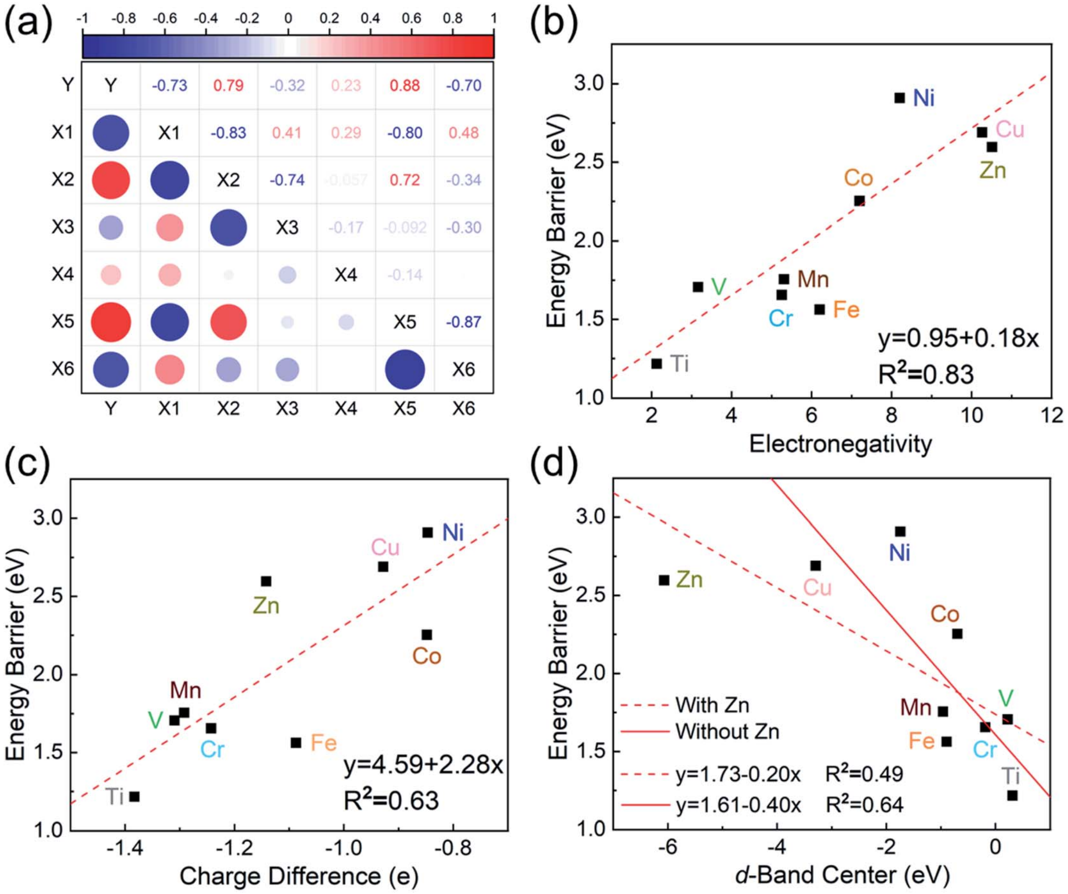

Fig. 3 (a) Correlation matrix of PCCs between material properties and the dehydrogenation energy barriers of $MgH_2$ upon addition of SACs. $Y$ is energy barrier, $X_1$ is the height of metal atoms, $X_2$ is the difference in the charge of metal atoms, $X_3$ is the difference in the charge of N, $X_4$ is H adsorption energy, $X_5$ is electronegativity, and $X_6$ is the d-band center. The value domain of PCCs is [−1,1]. The size of the circle represents the size of its corresponding PCC values. Blue and red indicate positive and negative correlations, respectively. (b–d) Correlations of (b) electronegativity *vs.* energy barrier, (c) metal charge difference *vs.* energy barrier, and (d) metal d-band center *vs.* energy barrier. The red dotted line represents the fitted curve with all data, while the red solid line represents the fitted curve without the outlier SACs–Zn.

experimental methods might unavoidably lead to different N-coordination numbers and environments for the doped transition metals, leading to uncertainty in the analyses. Being very different from the analytical methods used in previous studies, herein, we for the first time performed first-principles based analysis on this SAC–$MgH_2$ system with an explicit stable metal–$N_4$–C structure. Throughout the calculations, Fe is an outlier for several reasons. For example, in different coordination and experimental environments, Fe may present different magnetic states.[102,103] In addition, in previous studies, hydrides are easily formed at the sites associated with Fe,[104–107] having different properties compared to many other transition metals. Fig. 3c shows the Bader charges of metals after relaxation and the difference in the intrinsic charges of metal atoms. We found that there is a linear correlation between the metal charge difference and dehydrogenation performance. Therefore, we speculate that its ability to optimize dehydrogenation is related to the charge properties of metal atoms. Therefore, we further calculated the d-band centers (*i.e.*, average energy of d-electrons) of the single-atom metals (Fig. 3d), which closely correlate with the dehydrogenation performance of SACs. Other correlation analyses are shown in Fig. S2.† According to the classic d-band center theory,[89] a surface site with a more positive d-band center has a stronger adsorption capacity. This is in good agreement with our findings that the single-atom metal sites with more positive d-band centers generally have lower barriers for the reaction because of the stronger attractive interaction with the atomic H from $MgH_2$.

Based on all the analyses above, we can find that the dehydrogenation performance of $MgH_2$ can be significantly improved upon adding SACs, where the electronegativity of the single-atom system plays a key role in determining the performance. To further illustrate the electronic changes upon adding SACs, we analyzed the electron localization functions (ELFs) of both $MgH_2$ and $MgH_2$/SACs (Fig. 4, S3 and S4†). Red color indicates a higher degree of electron localization, while blue color indicates a lower electron density in the region. From all the ELF results, we can see that the electron localization degree around H is high on the pure $MgH_2$ system, while it decreases upon the addition of SACs above the $MgH_2$ surface. The phenomenon that the degree of electron localization decreases not only occurs on surface H but also slightly on the sublayer H. This suggests that SACs affect not only the electronic properties of surface H but also the sublayer H of $MgH_2$. The decrease in the degree of electron-domain fixation indicates that the addition of SACs makes it easier for the electrons around the atomic H to leave $MgH_2$.

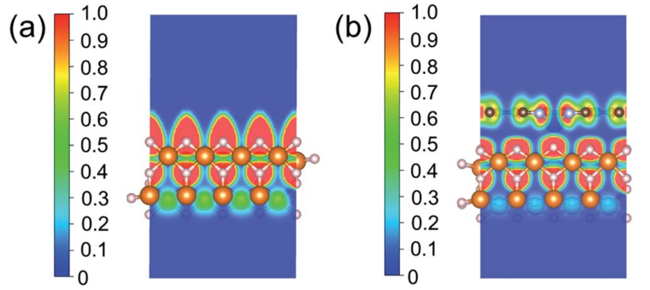

Fig. 4 ELFs of (a) $MgH_2$ and (b) $MgH_2$/SACs–Ti. The section is the 010 plane of the H atom nearest to the metal atom. In the color bars, 1 represents a fully localized state, 0.5 represents a uniform electronic gas state, and 0 represents a fully nonlocalized state. The ELF results of other $MgH_2$/SAC systems are shown in Fig. S4.†

Furthermore, the charge changes of $MgH_2$ induced by the addition of SACs were analyzed in detail by calculating the charge density difference (Fig. 5a–i). Charge transfer occurs on the atomic H closest to the transition metal, and the charge is obtained by losing electrons above H. As mentioned earlier in this paper, atomic H has a negative charge in $MgH_2$, and the addition of catalyst may tune its charge properties. Fig. 5 shows the positions of electron aggregation and reduction, which helps understand the charge changes upon the addition of SACs. Interestingly, as the corresponding dehydrogenation barrier decreases, the charge migration of H becomes less significant. For those systems which have lower dehydrogenation barriers (*e.g.*, $MgH_2$/SAC–Ti), the yellow region illustrates the clustering of H electrons due to the influence of SACs, while the blue region indicates that the aggregated electrons are provided by electrons in the bonding orbitals between H and Mg below. This indicates that the Mg–H bond is not stable because the electrons from H migrate toward the transition metal atom, in turn reducing the dehydrogenation barrier of $MgH_2$. Graphene is very stable due to the largely delocalized π-bonding, thus it does not provide electrons to hydrogen. However, N will compete with H for the valence electrons of metal. When the N–metal bond is weaker, the single-atom metal will be closer to $MgH_2$. Then more electrons will move closer to H. These phenomena are generally consistent among the analyzed 3d transition metals. Furthermore, we analyzed the electronic changes of metal atoms by calculating the projected density of states (PDOS) of d electrons of the systems (Fig. S5†). The distribution changes of the d-states upon the combination of SACs and $MgH_2$ are qualitatively consistent with the calculated charge density differences in Fig. 5. These further confirm that the interactions between SACs and $MgH_2$ significantly influence material performance.

### AIMD simulations

The desorption ability of hydrogen in the system is an important factor for measuring the performance of hydrogen storage materials. Therefore, we analyze the hydrogen desorption performance of $MgH_2$ before and after adding SACs using AIMD simulations. Previous MD simulations found that $MgH_2$ dehydrogenates only when MD simulations were performed at temperatures above 663 K.[84] Therefore, we set the temperature to 500 K in our AIMD simulations. After analyzing both $MgH_2$ and $MgH_2$/SACs–Ti for 10 ps, we found that the H-atoms become more confused with the addition of SAC in the animation of AIMD results. Therefore, the root mean square displacement/deviation (RMSD) of H in the whole system was chosen as an important indicator.[108] The shift of H increases significantly and slightly fluctuates with the addition of SACs

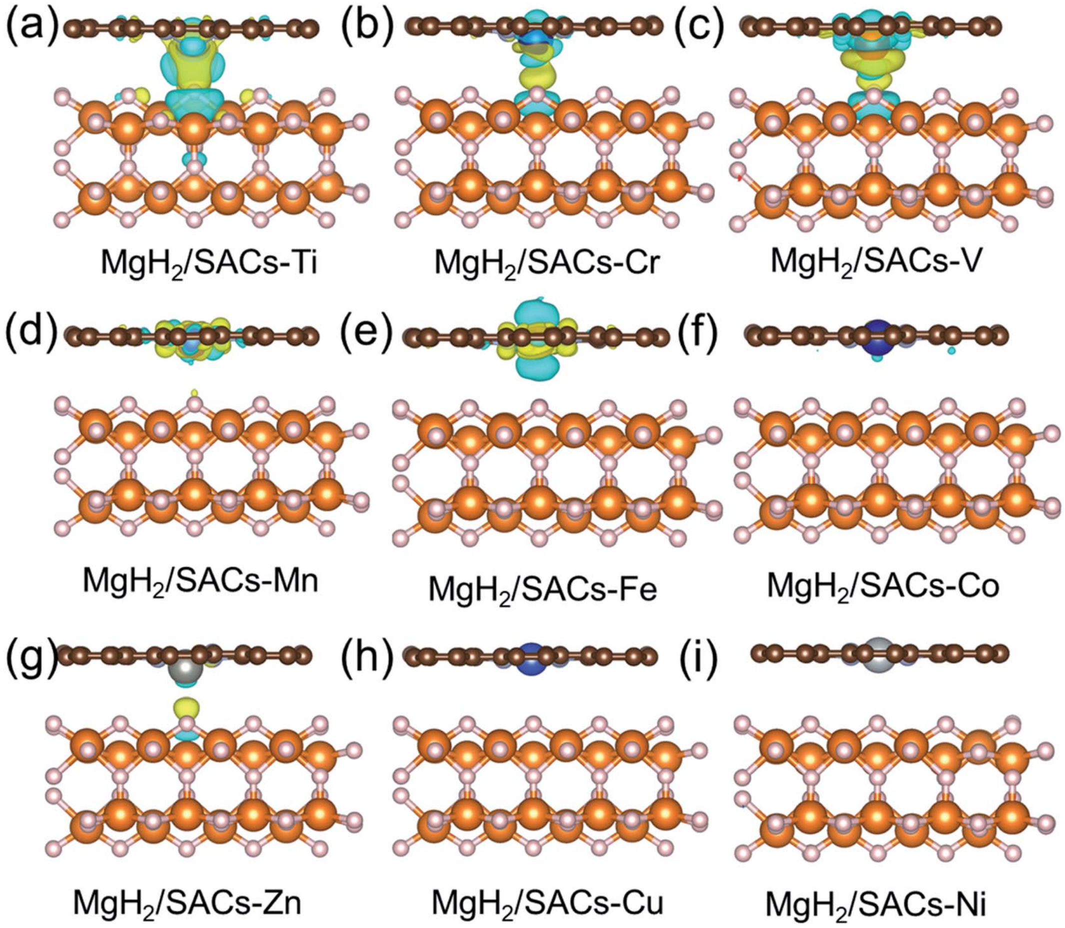

**Fig. 5** (a–i) Calculated charge density differences of $MgH_2$/SACs–TM (TM = Ti, V, Cr, Zn, Cu, Mn, Co, Fe, and Ni) induced by the addition of SACs. The yellow and blue isosurfaces indicate electron accumulation and loss, respectively. All the results are plotted with an isovalue of 0.001 e $Å^{-3}$. White, orange, brown, and gray spheres represent H, Mg, C, and N, respectively.

(Fig. 6a), indicating that H in $MgH_2$ desorbs more easily with the addition of SACs above. To better analyze the displacement and diffusion of H in each part of $MgH_2$, we plotted the displacement (Fig. 6a) and diffusion rates (Fig. 6c) of H in each layer and observed the corresponding structures. As shown in Fig. 6b, we divided the layers for the atomic H in $MgH_2$. In Fig. 6a–c, we can find that the diffusion rate of atomic H away from the surface is greater than that of surface H. For Fig. 6c, the diffusion coefficient ($D$) was calculated by converting RMSD to mean square displacement (MSD):

$$D = \lim_{t \to \infty} \left[ \frac{1}{2dt} \left\langle \left[ \vec{r}(t) \right]^2 \right\rangle \right] \tag{7}$$

where $d$ is the dimension ($d = 3$), $\vec{r}(t)^2$ is MSD, and $t$ is simulation time.[109] Fig. 6c clearly shows the change of H diffusivity after adding SAC–Ti. First, the diffusion rate at 10 ps on the right is several orders of magnitude higher than that on the left. Secondly, for pure $MgH_2$, diffusivity decreases with the increase of the number of layers, while that of the heterojunction increases with the increase of the number of layers. It indicates that the addition of catalyst affects the deep H atoms, which is consistent with the results of the above ELF analysis. However, we can confirm that SACs–Ti can significantly increase H diffusivity. We selected several extreme fluctuating points and observed the differences between the two structures (Fig. 6d and e). It can be seen that an H atom breaks the chemical bond with a Mg, and this H atom forms a new chemical bond with Ti. However, pure $MgH_2$ does not change much at this temperature, H is not detached and the vibration amplitude is not very large. As mentioned earlier in this paper, N prevents H from attracting the valence electrons provided by the single-atom metal. When Mg approaches N, it can provide valence electrons to N, which in turn weakens and subsequently breaks the Mg–H bond, thus enhancing the dehydrogenation capacity.

## Bonding analysis

Motivated by the above analyses, herein, we further analyze the Mg–H bonding information by calculating the integrated crystal orbital Hamilton population (ICOHP) integral values of the Mg–H bond (Tables S7–S10†) based on the COHP method (Fig. 7).[90,91] Without SACs, the COHP distribution for two bridge Mg–H bonds of $MgH_2$ are the same and no anti-bonding orbitals are occupied, indicating that Mg–H bonds are stabilized by the electrons of H (1s)–Mg (3s) (Fig. 7a and b).

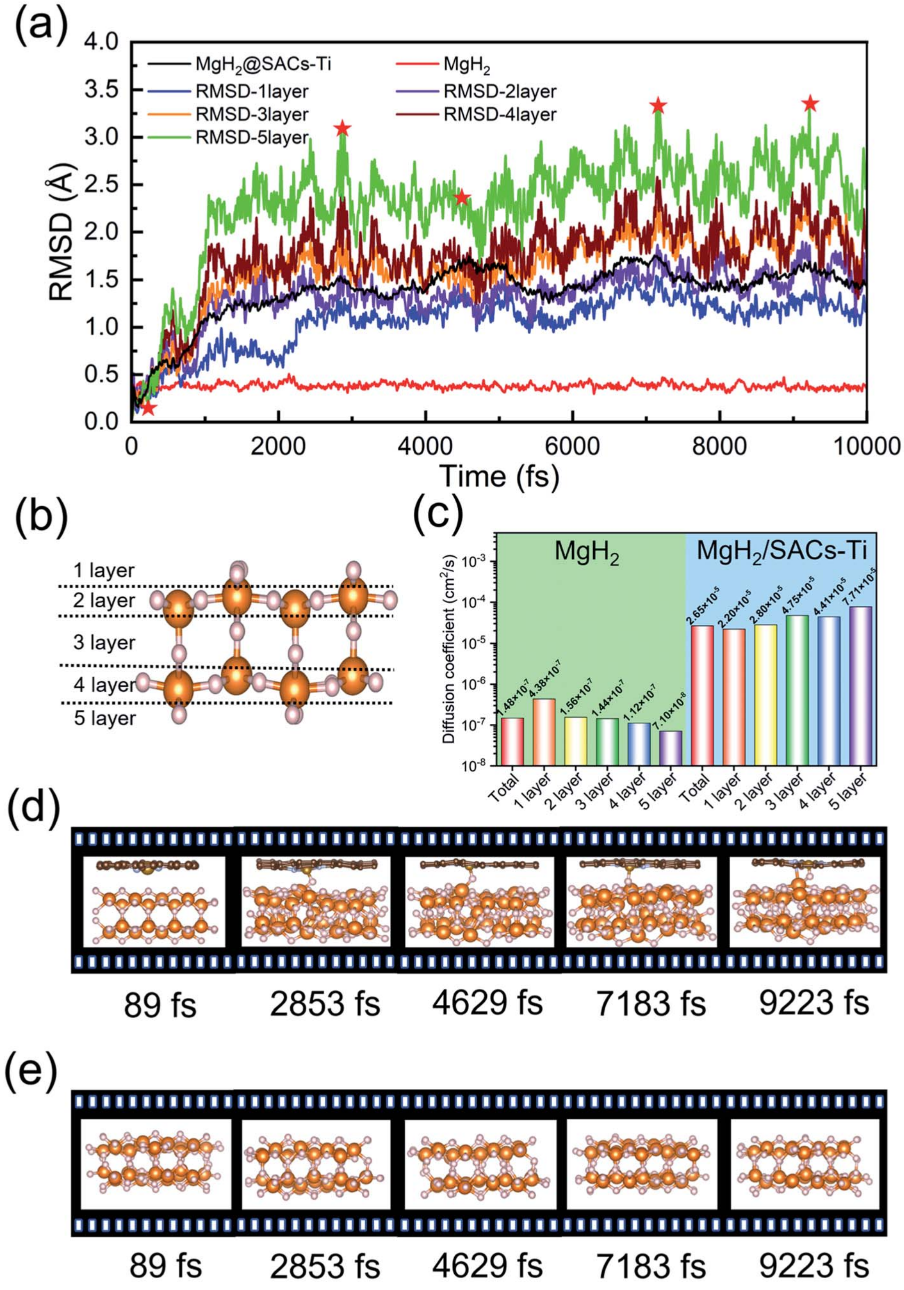

Fig. 6 AIMD simulation results on $MgH_2$ and $MgH_2$/SACs–Ti. (a) RMSD changes of atomic H before and after the addition of SACs–Ti. (b) Descriptions of the layers in $MgH_2$. White, orange, brown, gray, and golden spheres represent H, Mg, C, N, and Ti, respectively. In (a), the red curve is the RMSD of pure $MgH_2$; the black curve is the RMSD after the addition of SACs–Ti. Red stars represent the structures shown in (d) and (e) for $MgH_2$ and $MgH_2$/SACs–Ti. (c) Comparison of H diffusivity in each layer of $MgH_2$ before and after the addition of SACs–Ti. (d) Structural changes of heterojunctions at 500 K after adding SACs–Ti within 10 ps. (e) Structural changes of pure $MgH_2$ at 500 K within 10 ps.

Obviously, there is anti-bonding orbital occupation in the bond of H (1s)–Mg (3s), as shown in the lower left of Fig. 7c and d, illustrating that the Mg–H bond of $MgH_2$ becomes very unstable after the addition of SACs. From Fig. 7e and f, the bond strength of Mg–H mainly depends on the electron distribution of H (1s)–Mg (3s). The integral values of ICOHP for bridge Mg–H bonds of $MgH_2$ with SACs are obviously smaller than those without SACs, providing direct evidence that SACs can efficiently promote the dehydrogenation of $MgH_2$ through weakening the Mg–H bond. In addition, we performed similar analyses for the Mg–H bond away from the Ti atom (Fig. S6†). We found that even though these bonds are far from the Ti atom, they still show a decrease in –IPCOHP. And still, some of the bonds show antibonding orbitals, indicating that the catalyst weakens most of the Mg–H bonds nearby. This suggests that the catalyst not only promotes the first $H_2$ dehydrogenation. Similar analyses of other heterojunctions are shown in Tables S11–S16.†

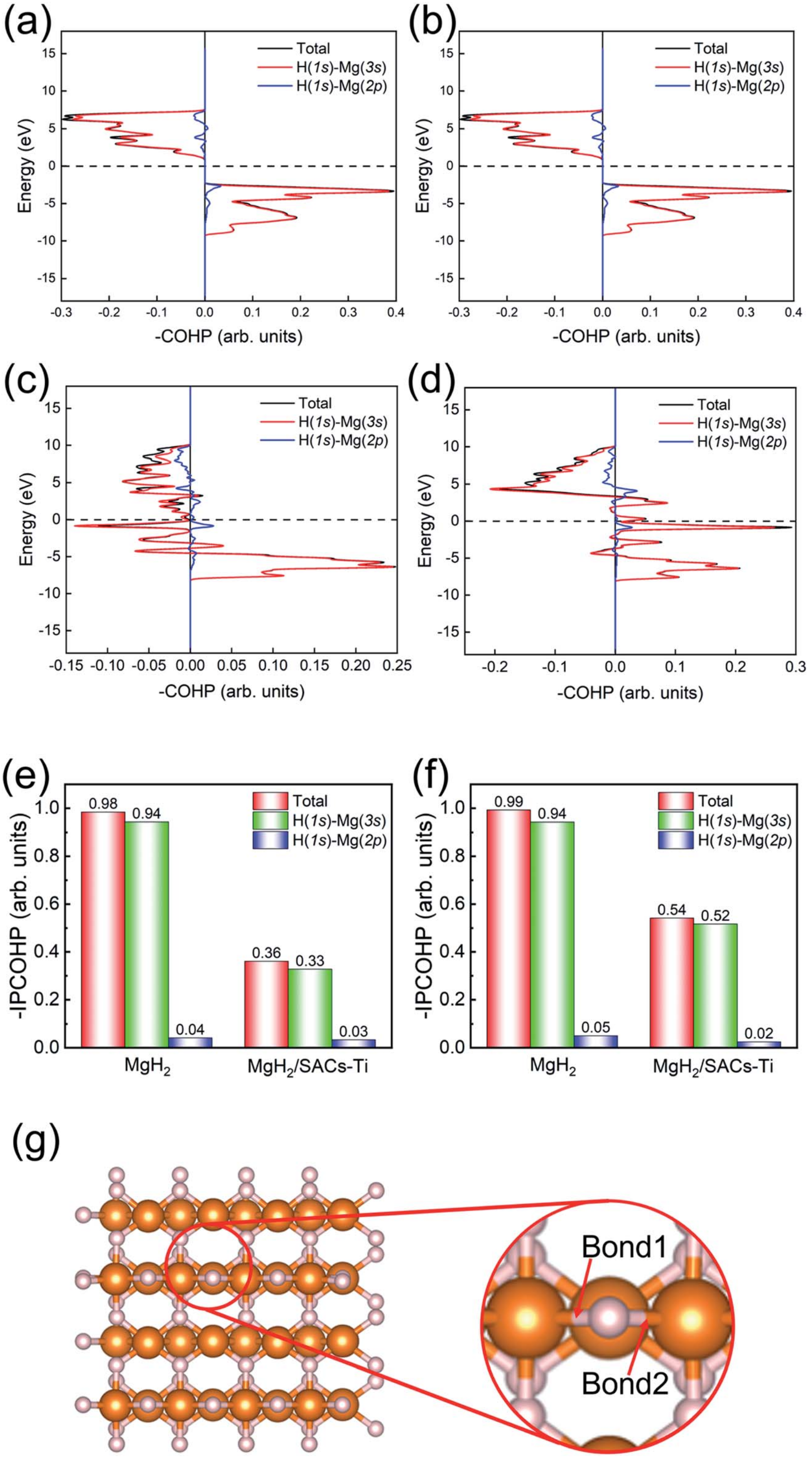

Fig. 7 (a and b) COHP analysis of the Mg–H bond 1 and bond 2 in $MgH_2$. (c and d) COHP analysis of the Mg–H bond 1 and bond 2 in $MgH_2$/SACs–Ti. (e and f) Comparison of the integral values of Mg–H bond 1 and bond 2 between $MgH_2$ and $MgH_2$/SACs–Ti in the systems. (g) Illustrations of the bond 1 and bond 2 in $MgH_2$. White and orange spheres represent H and Mg, respectively.

### Screening other SACs based on the linear scaling relation

As the final section of this study, we use the fitted correlation of energy barrier *vs.* electronegativity to predict the dehydrogenation performance of other $MgH_2$/SAC systems (Fig. 8). The detailed parameters are tabulated in Table S17.† Interestingly, Hf, Sc, Zr, and Y are predicted to be promising dopants of SACs due to their low system electronegativity. We expect that these predicted performances can provide further

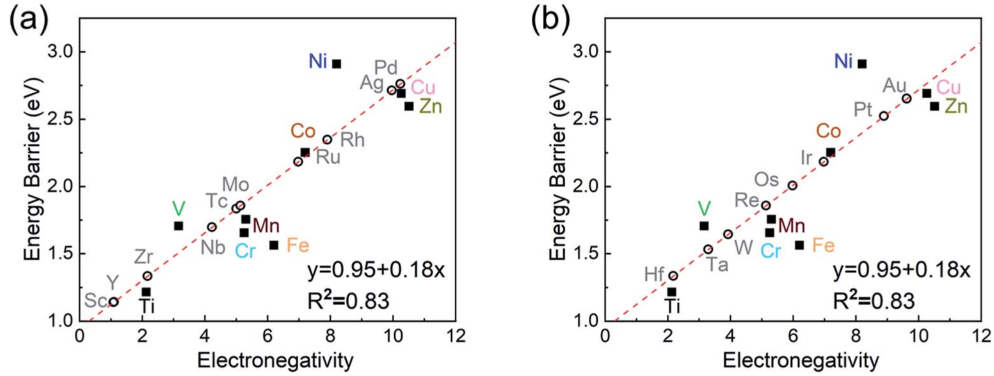

Fig. 8 Prediction of dehydrogenation energy barriers at $MgH_2$/SACs–TM based on the linear correlation of dehydrogenation barrier *vs.* electronegativity. The empty and solid dots represent the predicted and DFT-calculated values, respectively. In (a), the elements consist of Sc and 5d TMs: TM = Sc, Y, Zr, Nb, Mo, Tc, Ru, Rh, Pd, and Ag. In (b), the elements consist of 4d TMs: TM = Hf, Ta, W, Re, Os, Ir, Pt, and Au.

guideline and motivation for future experimental and theoretical studies.

## Conclusion

In summary, we explicitly analyzed $MgH_2$/SAC heterojunction systems including nine different 3d transition metals as potential hydrogen storage materials, using spin-polarized DFT-D3 calculations. We found that the energy barriers of $MgH_2$ dehydrogenation are significantly reduced by 0.51–2.22 eV through the promotion effects of a $MgH_2$/SAC heterojunction. Among them, $MgH_2$/SAC–Ti showed the best performance and was further analyzed. We found that the electronic properties of the single-atom metal play an essential role in determining the dehydrogenation performance of $MgH_2$/SACs. Using AIMD simulations, these promotion effects were unraveled based on the observation of H diffusivity. To provide further insights, ELFs, charge density difference, H adsorption energy, system electronegativity, d-band center, and COHP were comprehensively analyzed. Finally, we predicted the performance of eighteen other $MgH_2$/SACs based on the proven good linear scaling relation between system electronegativity and dehydrogenation barrier. For practical applications of $MgH_2$, hydrogen storage under conventional conditions can now be achieved by a simple ball milling process with $MgH_2$.[110] Based on the previous experimental success in the synthesis of such a heterojunction-$MgH_2$ system[73] and the emerging atomic-level control synthesis of a target N-coordination environment (*e.g.*, by developing a single-atom covalent organic framework structure),[50] we believe that the experimental synthesis is facile for realizing our designs based on current techniques. Most importantly, this study provides important design guidelines of novel $MgH_2$/SAC heterojunction materials and a solution to the sluggish kinetics of $MgH_2$ dehydrogenation in hydrogen storage.

## Conflicts of interest

There are no conflicts to declare.

## Acknowledgements

This work was supported by the National Natural Science Foundation of China (52006073 and 21703161), Natural Science Foundation of Hebei Province of China (E2020502023), and the Interdisciplinary Innovation Program of North China Electric Power University (Grant Number XM2112355).

## References

1 L. Schlapbach and A. Züttel, in *Materials for Sustainable Energy: A Collection of Peer-Reviewed Research and Review Articles from Nature Publishing Group*, World Scientific, 2011, pp. 265–270.
2 M. Ball and M. Wietschel, *Int. J. Hydrogen Energy*, 2009, **34**, 615–627.
3 R. Ramachandran and R. K. Menon, *Int. J. Hydrogen Energy*, 1998, **23**, 593–598.
4 Y. Luo, L. Sun, F. Xu and Z. Liu, *J. Mater. Chem. A*, 2018, **6**, 7293–7309.
5 Q. Lai, M. Paskevicius, D. A. Sheppard, C. E. Buckley, A. W. Thornton, M. R. Hill, Q. Gu, J. Mao, Z. Huang and H. K. Liu, *ChemSusChem*, 2015, **8**, 2789–2825.
6 I. Sreedhar, K. M. Kamani, B. M. Kamani, B. M. Reddy and A. Venugopal, *Renewable Sustainable Energy Rev.*, 2018, **91**, 838–860.
7 A. Züttel, *Mater. Today*, 2003, **6**, 24–33.
8 S. Niaz, T. Manzoor and A. H. Pandith, *Renewable Sustainable Energy Rev.*, 2015, **50**, 457–469.
9 D. Pukazhselvan, V. Kumar and S. K. Singh, *Nano Energy*, 2012, **1**, 566–589.
10 N. S. Norberg, T. S. Arthur, S. J. Fredrick and A. L. Prieto, *J. Am. Chem. Soc.*, 2011, **133**, 10679–10681.
11 F. Schüth, B. Bogdanović and M. Felderhoff, *Chem. Commun.*, 2004, 2249–2258.
12 X. Zhang, Y. Liu, X. Zhang, J. Hu, M. Gao and H. Pan, *Mater. Today Nano*, 2020, **9**, 100064.
13 L. Schlapbach and A. Züttel, *Nature*, 2001, **414**, 353–358.

14 G.-x. Liang, J. Huot, S. Boily, A. Van Neste and R. Schulz, *J. Alloys Compd.*, 1999, **292**, 247–252.
15 W. Grochala and P. P. Edwards, *Chem. Rev.*, 2004, **104**, 1283–1316.
16 W. Li, C. Li, H. Ma and J. Chen, *J. Am. Chem. Soc.*, 2007, **129**, 6710–6711.
17 M. Zhu, Y. Lu, L. Ouyang and H. Wang, *Materials*, 2013, **6**, 4654–4674.
18 H. Zhang, X. Zheng, T. Wang and X. Li, *Intermetallics*, 2016, **70**, 29–32.
19 X. Hou, R. Hu, T. Zhang, H. Kou and J. Li, *J. Power Sources*, 2016, **306**, 437–447.
20 X. Jiang, K. Fu, R. Xiao, Y. Wu, B. Sun, H. Shao, X. Wu, J. Zheng and X. Li, *J. Alloys Compd.*, 2018, **751**, 176–182.
21 M. Chen, X. Xiao, M. Zhang, M. Liu, X. Huang, J. Zheng, Y. Zhang, L. Jiang and L. Chen, *Int. J. Hydrogen Energy*, 2019, **44**, 1750–1759.
22 Y. Lu, H. Wang, J. Liu, L. Ouyang and M. Zhu, *J. Power Sources*, 2018, **396**, 796–802.
23 M. Liu, S. Zhao, X. Xiao, M. Chen, C. Sun, Z. Yao, Z. Hu and L. Chen, *Nano Energy*, 2019, **61**, 540–549.
24 A. Schneemann, J. L. White, S. Kang, S. Jeong, L. F. Wan, E. S. Cho, T. W. Heo, D. Prendergast, J. J. Urban and B. C. Wood, *Chem. Rev.*, 2018, **118**, 10775–10839.
25 G. Xia, Y. Tan, X. Chen, D. Sun, Z. Guo, H. Liu, L. Ouyang, M. Zhu and X. Yu, *Adv. Mater.*, 2015, **27**, 5981–5988.
26 E. S. Cho, A. M. Ruminski, Y. S. Liu, P. T. Shea, S. Kang, E. W. Zaia, J. Y. Park, Y. D. Chuang, J. M. Yuk and X. Zhou, *Adv. Funct. Mater.*, 2017, **27**, 1704316.
27 M. Ma, L. Yang, L. Ouyang, H. Shao and M. Zhu, *Energy*, 2019, **167**, 1205–1211.
28 N. Sazelee, N. Idris, M. M. Din, N. Mustafa, N. Ali, M. Yahya, F. H. Yap, N. Sulaiman and M. Ismail, *Int. J. Hydrogen Energy*, 2018, **43**, 20853–20860.
29 L.-P. Ma, X.-D. Kang, H.-B. Dai, Y. Liang, Z.-Z. Fang, P.-J. Wang, P. Wang and H.-M. Cheng, *Acta Mater.*, 2009, **57**, 2250–2258.
30 Y. Liu, H. Du, X. Zhang, Y. Yang, M. Gao and H. Pan, *Chem. Commun.*, 2016, **52**, 705–708.
31 A. Valentoni, G. Mulas, S. Enzo and S. Garroni, *Phys. Chem. Chem. Phys.*, 2018, **20**, 4100–4108.
32 M. Zhang, X. Xiao, X. Wang, M. Chen, Y. Lu, M. Liu and L. Chen, *Nanoscale*, 2019, **11**, 7465–7473.
33 J. Zhang, R. Shi, Y. Zhu, Y. Liu, Y. Zhang, S. Li and L. Li, *ACS Appl. Mater. Interfaces*, 2018, **10**, 24975–24980.
34 M. Yahya and M. Ismail, *J. Energy Chem.*, 2019, **28**, 46–53.
35 M. Ismail, N. Mustafa, N. Ali, N. Sazelee and M. Yahya, *Int. J. Hydrogen Energy*, 2019, **44**, 318–324.
36 X. Huang, X. Xiao, W. Zhang, X. Fan, L. Zhang, C. Cheng, S. Li, H. Ge, Q. Wang and L. Chen, *Phys. Chem. Chem. Phys.*, 2017, **19**, 4019–4029.
37 N. Ali, N. Idris, M. M. Din, M. Yahya and M. Ismail, *J. Alloys Compd.*, 2019, **796**, 279–286.
38 N. Sazelee, N. Idris, M. M. Din, M. Yahya, N. Ali and M. Ismail, *Results Phys.*, 2020, **16**, 102844.
39 D. Peng, Z. Ding, Y. Fu, Y. Wang, J. Bi, Y. Li and S. Han, *RSC Adv.*, 2018, **8**, 28787–28796.
40 X. Zhang, Z. Leng, M. Gao, J. Hu, F. Du, J. Yao, H. Pan and Y. Liu, *J. Power Sources*, 2018, **398**, 183–192.
41 S. Gao, X. Wang, H. Liu, T. He, Y. Wang, S. Li and M. Yan, *J. Power Sources*, 2019, **438**, 227006.
42 A. Wang, J. Li and T. Zhang, *Nat. Rev. Chem.*, 2018, **2**, 65–81.
43 H. Zhang, G. Liu, L. Shi and J. Ye, *Adv. Energy Mater.*, 2018, **8**, 1701343.
44 L. Zhang, A. Wang, W. Wang, Y. Huang, X. Liu, S. Miao, J. Liu and T. Zhang, *ACS Catal.*, 2015, **5**, 6563–6572.
45 H. Shen, E. Gracia-Espino, J. Ma, H. Tang, X. Mamat, T. Wagberg, G. Hu and S. Guo, *Nano Energy*, 2017, **35**, 9–16.
46 Y. Peng, B. Lu and S. Chen, *Adv. Mater.*, 2018, **30**, 1801995.
47 J. Masa, W. Xia, M. Muhler and W. Schuhmann, *Angew. Chem., Int. Ed.*, 2015, **54**, 10102–10120.
48 W. Liu, L. Zhang, X. Liu, X. Liu, X. Yang, S. Miao, W. Wang, A. Wang and T. Zhang, *J. Am. Chem. Soc.*, 2017, **139**, 10790–10798.
49 Y. Yang, Y. Yang, Z. Pei, K.-H. Wu, C. Tan, H. Wang, L. Wei, A. Mahmood, C. Yan and J. Dong, *Matter*, 2020, **3**, 1442–1476.
50 C. Liu, H. Li, F. Liu, J. Chen, Z. Yu, Z. Yuan, C. Wang, H. Zheng, G. Henkelman and L. Wei, *J. Am. Chem. Soc.*, 2020, **142**, 21861–21871.
51 Y. Zhou, J. Li, X. Gao, W. Chu, G. Gao and L.-W. Wang, *J. Mater. Chem. A*, 2021, **9**, 9979–9999.
52 H. Li, B. Yu, Z. Zhuang, W. Sun, B. Jia and T. Ma, *J. Mater. Chem. A*, 2021, **9**, 4184–4192.
53 B. Yu, H. Li, J. White, S. Donne, J. Yi, S. Xi, Y. Fu, G. Henkelman, H. Yu and Z. Chen, *Adv. Funct. Mater.*, 2020, **30**, 1905665.
54 M. Yan, L. Jasin Arachchige, A. Dong, X. L. Zhang, Z. Dai and C. Sun, *Inorg. Chem.*, 2021, **60**, 18314–18324.
55 Y. Kong, D. Liu, H. Ai, K. H. Lo, S. Wang and H. Pan, *ACS Appl. Nano Mater.*, 2020, **3**, 11274–11281.
56 Y. Kong, T. He, A. R. Puente Santiago, D. Liu, A. Du, S. Wang and H. Pan, *ChemSusChem*, 2021, **14**, 3257–3266.
57 C. Liu, Q. Li, J. Zhang, Y. Jin, D. R. MacFarlane and C. Sun, *J. Mater. Chem. A*, 2019, **7**, 4771–4776.
58 B. Zhang, B. Zhang, Y. Jiang, T. Ma, H. Pan and W. Sun, *Small*, 2021, **17**, 2101443.
59 S. Vijay, W. Ju, S. Brückner, S.-C. Tsang, P. Strasser and K. Chan, *Nat. Catal.*, 2021, **4**, 1024–1031.
60 Z. Li, R. Wu, S. Xiao, Y. Yang, L. Lai, J. S. Chen and Y. Chen, *Chem. Eng. J.*, 2022, **430**, 132882.
61 X. Shao, X. Yang, J. Xu, S. Liu, S. Miao, X. Liu, X. Su, H. Duan, Y. Huang and T. Zhang, *Chem*, 2019, **5**, 693–705.
62 Y. Ma, B. Chi, W. Liu, L. Cao, Y. Lin, X. Zhang, X. Ye, S. Wei and J. Lu, *ACS Catal.*, 2019, **9**, 8404–8412.
63 W. Liu, Y. Chen, H. Qi, L. Zhang, W. Yan, X. Liu, X. Yang, S. Miao, W. Wang and C. Liu, *Angew. Chem.*, 2018, **130**, 7189–7193.
64 X. He, Q. He, Y. Deng, M. Peng, H. Chen, Y. Zhang, S. Yao, M. Zhang, D. Xiao and D. Ma, *Nat. Commun.*, 2019, **10**, 1–9.
65 V. Fung, F. F. Tao and D.-e. Jiang, *Phys. Chem. Chem. Phys.*, 2018, **20**, 22909–22914.
66 V. Fung, F. Tao and D. e. Jiang, *ChemCatChem*, 2018, **10**, 244–249.

67 L. Zhang, Y. Jia, G. Gao, X. Yan, N. Chen, J. Chen, M. T. Soo, B. Wood, D. Yang and A. Du, *Chem*, 2018, **4**, 285–297.

68 M. Sun, J. Ji, M. Hu, M. Weng, Y. Zhang, H. Yu, J. Tang, J. Zheng, Z. Jiang and F. Pan, *ACS Catal.*, 2019, **9**, 8213–8223.

69 J. Park, S. Lee, H. E. Kim, A. Cho, S. Kim, Y. Ye, J. W. Han, H. Lee, J. H. Jang and J. Lee, *Angew. Chem., Int. Ed.*, 2019, **58**, 16038–16042.

70 H.-W. Liang, S. Brüller, R. Dong, J. Zhang, X. Feng and K. Müllen, *Nat. Commun.*, 2015, **6**, 1–8.

71 J. Yan, Y. Ji, M. Batmunkh, P. An, J. Zhang, Y. Fu, B. Jia, Y. Li, S. Liu and J. Ye, *Angew. Chem., Int. Ed.*, 2021, **60**, 2541–2547.

72 V. Fung, G. Hu, Z. Wu and D.-e. Jiang, *J. Phys. Chem. C*, 2020, **124**, 19571–19578.

73 Y. Huang, C. An, Q. Zhang, L. Zang, H. Shao, Y. Liu, Y. Zhang, H. Yuan, C. Wang and Y. Wang, *Nano Energy*, 2021, **80**, 105535.

74 G. Kresse and D. Joubert, *Phys. Rev. B: Condens. Matter Mater. Phys.*, 1999, **59**, 1758.

75 J. P. Perdew, K. Burke and M. Ernzerhof, *Phys. Rev. Lett.*, 1996, **77**, 3865.

76 G. Kresse and J. Furthmüller, *Phys. Rev. B: Condens. Matter Mater. Phys.*, 1996, **54**, 11169.

77 J. Wellendorff, T. L. Silbaugh, D. Garcia-Pintos, J. K. Nørskov, T. Bligaard, F. Studt and C. T. Campbell, *Surf. Sci.*, 2015, **640**, 36–44.

78 H. Zheng, H. Li, W. Song, Z. Zhao and G. Henkelman, *J. Phys. Chem. C*, 2021, **125**, 12028–12037.

79 A. D. Becke and E. R. Johnson, *J. Chem. Phys.*, 2005, **122**, 154104.

80 S. Grimme, J. Antony, S. Ehrlich and H. Krieg, *J. Chem. Phys.*, 2010, **132**, 154104.

81 G. Henkelman and H. Jónsson, *J. Chem. Phys.*, 2000, **113**, 9978–9985.

82 G. Henkelman, B. P. Uberuaga and H. Jónsson, *J. Chem. Phys.*, 2000, **113**, 9901–9904.

83 G. Kresse and J. Hafner, *J. Non-Cryst. Solids*, 1993, **47**, 558.

84 M. Lakhal, M. Bhihi, A. Benyoussef, A. El Kenz, M. Loulidi and S. Naji, *Int. J. Hydrogen Energy*, 2015, **40**, 6137–6144.

85 W. F. Humphrey, A. Dalke and K. Schulten, *J. Mol. Graphics*, 1996, **14**(33–38), 27–38.

86 P. Hnggi, P. Talkner and M. Borkovec, *Rev. Mod. Phys.*, 1990, **62**, 251–341.

87 W. Yang, S. Xu, K. Ma, C. Wu, I. D. Gates, X. Ding, W. Meng and Z. Gao, *Nano Mater. Sci.*, 2020, **2**, 120–131.

88 H. Xu, D. Cheng, D. Cao and X. C. Zeng, *Nat. Catal.*, 2018, **1**, 339–348.

89 B. Hammer and J. K. Norskov, *Nature*, 1995, **376**, 238–240.

90 V. L. Deringer, A. L. Tchougréeff and R. Dronskowski, *J. Phys. Chem. A*, 2011, **115**, 5461–5466.

91 R. Dronskowski and P. E. Bloechl, *J. Phys. Chem.*, 1993, **97**, 8617–8624.

92 S. Maintz, V. L. Deringer, A. L. Tchougréeff and R. Dronskowski, *J. Comput. Chem.*, 2016, **37**, 1030–1035.

93 S. Maintz, V. L. Deringer, A. L. Tchougréeff and R. Dronskowski, *J. Comput. Chem.*, 2013, **34**, 2557–2567.

94 A. Du, S. C. Smith, X. Yao and G. Lu, *Surf. Sci.*, 2006, **600**, 1854–1859.

95 Q. Li, S. Qiu, C. Wu, K. T. Lau, C. Sun and B. Jia, *J. Phys. Chem. C*, 2021, **125**, 2357–2363.

96 J. J. Liang, *J. Alloys Compd.*, 2007, **446**, 72–79.

97 L. L. Wang and D. D. Johnson, *J. Phys. Chem. C*, 2012, **116**, 7874–7878.

98 M. Lakhal, M. Bhihi, A. Benyoussef, A. El Kenz, M. Loulidi and S. Naji, *Int. J. Hydrogen Energy*, 2015, **40**, 6137–6144.

99 A. G. Asuero, A. Sayago and A. Gonzalez, *Crit. Rev. Anal. Chem.*, 2006, **36**, 41–59.

100 H. Wu, Z. Chen, Y. Wang, E. Cao, F. Xiao, S. Chen, S. Du, Y. Wu and Z. Ren, *Energy Environ. Sci.*, 2019, **12**, 2697–2705.

101 W. Yang, S. Xu, M. Kai, C. Wu and Z. Gao, *Nano Mater. Sci.*, 2019, **2**, 120–131.

102 A. Cao, V. J. Bukas, V. Shadravan, Z. Wang, H. Li, J. Kibsgaard, I. Chorkendorff and J. K. Nørskov, *Nat. Commun.*, 2022, **13**, 1–7.

103 M. Uhl, L. M. Sandratskii and J. Kübler, *J. Magn. Magn. Mater.*, 1992, **103**, 314–324.

104 Y.-C. Liu, K.-T. Chu, R.-L. Jhang, G.-H. Lee and M.-H. Chiang and, *Chem. Commun.*, 2013, **49**, 4743–4745.

105 F. Aubertin, U. Gonser and S. J. Campbell, *J. Phys. F: Met. Phys.*, 1984, **14**, 2213.

106 J. I. V. D. Vlugt, T. B. Rauchfuss, C. M. Whaley and S. R. Wilson, *J. Am. Chem. Soc.*, 2005, **127**, 16012–16013.

107 D. A. Papaconstantopoulos and A. C. Switendick, *J. Less-Common Met.*, 1982, **88**, 273–281.

108 K. Kobayashi and M. U. Salam, *Agron. J.*, 2000, **92**, 345–352.

109 J. Kubečka, F. Uhlík and P. Košovan, *Soft Matter*, 2016, **12**, 3760–3769.

110 H. Shao, G. Xin, Z. Jie, X. Li and E. Akiba, *Nano Energy*, 2012, **1**, 590–601.